How to cite: *Angew. Chem. Int. Ed.* **2024**, *63*, e202415624
doi.org/10.1002/anie.202415624

Covalent Organic Frameworks

A Covalent Triazine Framework for Photocatalytic Anti-Markovnikov Hydrofunctionalizations

Rakesh Maiti[+], Jeet Chakraborty[+], Prakash Kumar Sahoo, Ipsita Nath, Xingchao Dai, Jabor Rabeah, Nathalie De Geyter, Rino Morent, Pascal Van Der Voort, and Shoubhik Das**

Dedicated to Prof. Rhett Kempe on the occasion of his 60th birthday.

Abstract: Porous materials-based heterogeneous photocatalysts, performing selective organic transformations, are increasing the applicability of photocatalytic reactions due to their ability to merge traditional photocatalysis with structured pores densely decorated with catalytic moiety for efficient mass and charge transfer, as well as added recyclability. We herein disclose a porous crystalline covalent triazine framework (CTF)-based heterogeneous photocatalyst that exhibits excellent photoredox properties for different hydrofunctionalization reactions such as hydrocarboxylations, hydroamination and hydroazidations. The high oxidizing property of this CTF enables the activation of styrenes, followed by regioselective C–N and C–O bond formation at ambient conditions. A change in the physicochemical and optoelectronic properties of the CTF, upon protonation during catalysis, lies at the basis of its photocatalytic properties. This allows us to obtain hydrocarboxylations, hydroamination, and hydroazidations from a myriad of electron-donating and -withdrawing aromatic and aliphatic substrates. This catalytic approach is further extended to late-stage functionalization of bio-active molecules. Finally, detailed characterizations of the CTF and further mechanistic investigations provide mechanistic insights into these reactions.

Introduction

In recent years, conjugated porous organic networks have emerged as an attractive class of sustainable heterogeneous photocatalysts.[1] Strong efforts have been made to develop a wide range of such materials for a myriad of photoredox-mediated organic transformations such as C–N cross-coupling,[7] [3+2] cycloaddition,[8] C–H functionalization,[9] oxidation,[10] and many more.[2, 12, 17] Covalent triazine frameworks (CTFs), a class of porous organic networks, offer great prospects in this regard owing to their high chemical stability, permanent nano-porosity, and robust backbone.[23, 35] Expediently, the structural and photophysical properties of the CTFs can be modulated via modification of the monomers' structure, which further adds to the customizability of the CTFs. For instance, in 2019, Banerjee *et al.* used a CTF, synthesized from melamine and 2,4,6-triformylphloroglucinol aldehyde, for the visible-light-mediated E–Z isomerization of olefins.[43] In addition, formation of C–C/C–P bonds,[44] C–C/C–O,[45] [2+2+2] cycloaddition,[46] and alcohol oxidation[47] have also been achieved by selecting appropriate monomers to derive photoactive CTFs. In 2021, the Bai group showed that the introduction of a π-cross-linker (acetylene) into the monomer of a CTF could enhance its photocatalytic potential, specifically for the oxidative coupling of amines with O_2 under light irradiation.[48] Beyond their utility in organic synthesis, CTFs with well-suited monomers have also proven to be an efficient platform for facilitating visible light-mediated activation of small molecules such as H_2O splitting,[19, 49] CO_2 reduction.[52] To this end, this highly promising strategy of CTF customization enabled us to achieve even more challenging reactions which was earlier only possible using expensive homogeneous photocatalysts.[55]

Visible-light-mediated hydrofunctionalizations of alkenes into valuable molecules are prototypal reactions that have exhibited promising advances in recent years. Because of the inclusion of radical pathway, this strategy enables us to alter the selectivity in the final products. Particularly, more challenging anti-Markovnikov products can be ob-

[*] Dr. R. Maiti,[+] P. Kumar Sahoo, Prof. S. Das
Department of Chemistry, University of Antwerp, Antwerp, Belgium
E-mail: shoubhik.das@uni-bayreuth.de
Dr. R. Maiti,[+] Prof. S. Das
Department of Chemistry, University of Bayreuth, Bayreuth, Germany
Dr. J. Chakraborty,[+] Dr. I. Nath, Prof. P. Van Der Voort
Department of Chemistry, Center for Ordered Materials, Organometallics and Catalysis, Ghent University, Ghent, Belgium
E-mail: pascal.vandervoort@ugent.be
X. Dai, J. Rabeah
Leibniz-Institut für Katalyse e. V. ander Universität Rostock (LIKAT), Albert-Einstein-Str.29a, 18059, Rostock, Germany
Prof. N. De Geyter, Prof. R. Morent
Department of Applied Physics, Research Unit Plasma Technology, Ghent University, Ghent, Belgium
[+] Equally contributed to this work.

tained over the traditional Markovnikov addition products. In these reactions, styrenes and their derivatives are routinely used as key building blocks to access structural complexity in a rapid and atom-economic fashion.[57] Mechanistically, a photocatalyst first oxidizes the styrene and generates the corresponding radical cation (Figure 1a).[64] Later, the electronic and thermodynamic parameters of the radical cation govern the nucleophilic addition to generate a regioselective functionalized product (Figure 1a). Notably, the success of this strategy entirely depends on the first step, i.e., the generation of the corresponding radical cation from the styrene. Thus, the photocatalyst must possess a high oxidation potential to commence this reaction since the derivatives of styrene have oxidation potentials in the range of ca. +1.6–+2.0 V *vs* SCE. Due to this constraint, only a limited number of photocatalysts are reported in the literature that can enable the direct oxidation of the styrene scaffold. For example, Stephenson et *al.* employed Ir[(dF-(CF_3ppy)$_2$)(5,5′-CF_3-bpy)] PF_6 [$E_{1/2}(M^+/M^*) = +1.68$ V *vs* SCE] to perform the oxidative amination of styrenes (Figure 1b).[66] Recently, the group of Pospech has developed a pyrimidopteridine-based photoredox catalyst which oxidized stilbene to the corresponding radical cation ($E_{1/2}(C^*/C^-) = +2.15$ V *vs* SCE).[67] In 1989, Otsuji *et al.* used 9,10-dicyanoanthracene (DCA) to accomplish the photoaddition of methanol to styrene.[69] Nevertheless, in this regard, acridinium salts are pioneer due to their high oxidation potentials (+1.88–2.19 V *vs* SCE) which allow them to promote the oxidation of the styrene and followed by this, facile addition of various nucleophiles in an anti-Markovnikov fashion.[70] The research groups of Lei, Yoon, Tang, and particularly, Nicewicz individually have achieved immense success with these acridinium salts by coupling a wide range of nucleophiles such as carboxylic acid, amine, azide, fluoride, chloride, sulfinic acid, phosphoric acid, and water to styrene derivatives.[73] Furthermore, modification of these salts [Such as-MesAcr$^+$-Ph 1: $E_{1/2}(C^*/C^-) = +2.15$ V *vs* SCE; MesAcr$^+$-Ph 2: $E_{1/2}(C^*/C^-) = +2.09$ V *vs* SCE; Figure 1b] empowered them to even validate direct aminations, fluorination of aromatics (even possess higher oxidation potential than styrene).[83] Despite such diverse abilities of these Ir-based and acridine-based photocatalysts, the higher price, and non-recyclability of these photocatalysts are the major challenges for their direct applications in the industrial scale (Figure 1b and Figure S1 in supplemental information).

We rationalized that a CTF could be an ideal photocatalyst to replace these expensive and non-recyclable homogeneous photocatalysts to make these processes more environmentally and industry friendly. However, a high oxidation potential at the valence band (VB) of CTF is necessary to achieve this. We hypothesized that employing an organic moiety which manifests high oxidative potential, might afford the corresponding CTF with a high valence band potential at par with the acridinium and Ir-based photocatalysts.[17] Particularly, we argued that hexaazatrinaphthylene (HATN), which is well-known for its high oxidation potential, *p*-type nature, and low cost, could be the ideal choice as a building block to obtain the deemed high-oxidizing CTF (HATN-CTF, Figure 1c and Figure S1

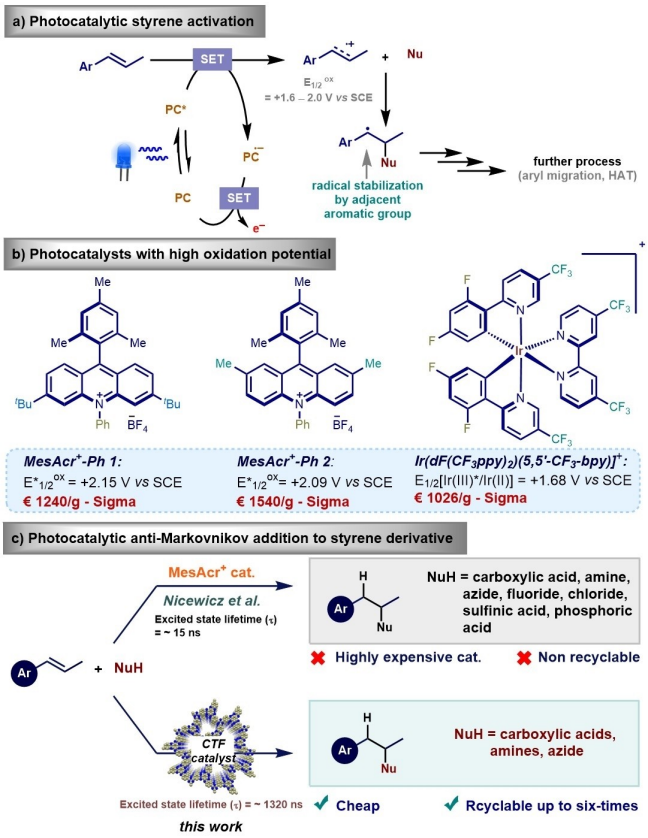

Figure 1. Photoredox catalysis with CTF and others.

in supplemental information).[86] Of note, HATN and similar hexaaza-molecules are well-known in literature due to their selective metal chelating ability. This property of the moieties together with their stable multi-redox states has been extensively explored in in the field of reversible metal-ion batteries and single-atom catalysis.[88]

Based on this premise, we herein report, for the first time, a merger of the super-oxidizing property of HATN and CTF-based heterogeneous photocatalyst which replaces the expensive, homogeneous, and high oxidizing photocatalysts. Furthermore, the application potential of HATN-CTF is demonstrated by applying the anti-Markovnikov addition of carboxylic acids, amines, and azide to styrene derivatives (C–O, C–N bond formation, Figure 1c). Additionally, the in situ reversible structural change in the HATN-CTF during photocatalysis, and its effect on the physicochemical properties of the material and its catalytic propensity have been investigated. We strongly believe that this strategy will become highly useful to replace other expensive homogeneous photocatalytic approaches and should open a new door to access unlimited possibilities.

Results and Discussion

At the outset of the project, HATN-CTF was synthesized via triflic acid-catalyzed cyclotrimerization of the nitrile functionalities present in the monomer, HATN-CN_3, into

triazine (Figure 2a).[93] CTF synthesis was confirmed by the Fourier transformed infrared (FTIR) spectroscopy. The FTIR peak at 2233 cm^{-1}, which belongs to the nitrile moieties present in the monomer, completely disappeared in the final CTF, suggesting their conversion to triazine (Figure S2 in supplemental information). Furthermore, the appearance of the distinct C=N stretching peaks for triazine at 1400–1700 cm^{-1} range endorsed the successful polymerization. Additionally, the powder X-ray diffraction (XRD) analysis revealed the crystalline nature of HATN-CTF (Figure 2b). We hypothesized that the large planar structure and significant intermolecular π–π stacking of the HATN monomers allowed them to be molecularly ordered in the reaction mixture. This led to the augmented crystallinity of the final CTF network. Similar phenomena of molecular ordering-induced crystallinity have been recently reported by other groups as well.[95] The experimentally obtained XRD pattern exhibited two relatively sharp peaks at 6.5° and 26.5° (2θ) corresponding to the (110) and (111) crystal plane diffractions, respectively. Another small intensity peak was observed at 14.3°, which can be ascribed to the diffraction form (220) crystal plane. The experimental diffractogram showed good agreement with the simulated XRD of the DFT optimized *a priori* model (Figure 2b, 2c, cf. supplemental information), where the peaks originating from the crystal planes of the AA stacked HATN-CTF can be recognized. On the other hand, the diffraction patterns of the AB-stacked model differed from the experimental XRD (Figure S3 in supplemental information). This additionally endorses our hypothesis of the in situ molecular ordering-induced polymerization of the monomers. Of note, some amorphous traits of the CTF can be observed in the experimental XRD as well.

The formation of HATN-CTF was further confirmed by solid-state 13 C CP-MAS NMR spectroscopy and X-ray photoelectron spectroscopy (XPS). A sharp peak can be seen at ca. 170 ppm in the NMR spectrum, which can be ascribed to the carbons in the triazine ring. On the other hand, no NMR peak can be seen at the 110–115 ppm region, where nitrile carbon usually appears (Figure 2f). This observation further endorsed the complete conversion of the nitriles to triazine during CTF formation. The conversion of cyanide to triazine was also validated by XPS core-level spectra. The C1s XPS pattern can be deconvoluted into three peaks, originating from C=C/C–H, C=N, and π–π* respectively (Figure 2e). Corresponding N1s core level XPS also showed only one sharp peak originating from C=N, whereas no XPS peaks corresponding to C≡N can be observed (Figure 2d). Compared to this, the deconvoluted C1s and N1s XPS of HATN-CN_3 showed an additional signal arising from the nitrile functionality (Figure S4 in supplemental information), further endorsing successful conversion of the monomer to corresponding CTF network.

A theoretical pore diameter of 1.50 nm was calculated from the DFT-optimized model of HATN-CTF which suggested a microporous nature of the material. As an experimental corroboration, the surface area and porosity of the CTF were experimentally determined by the N_2-sorption

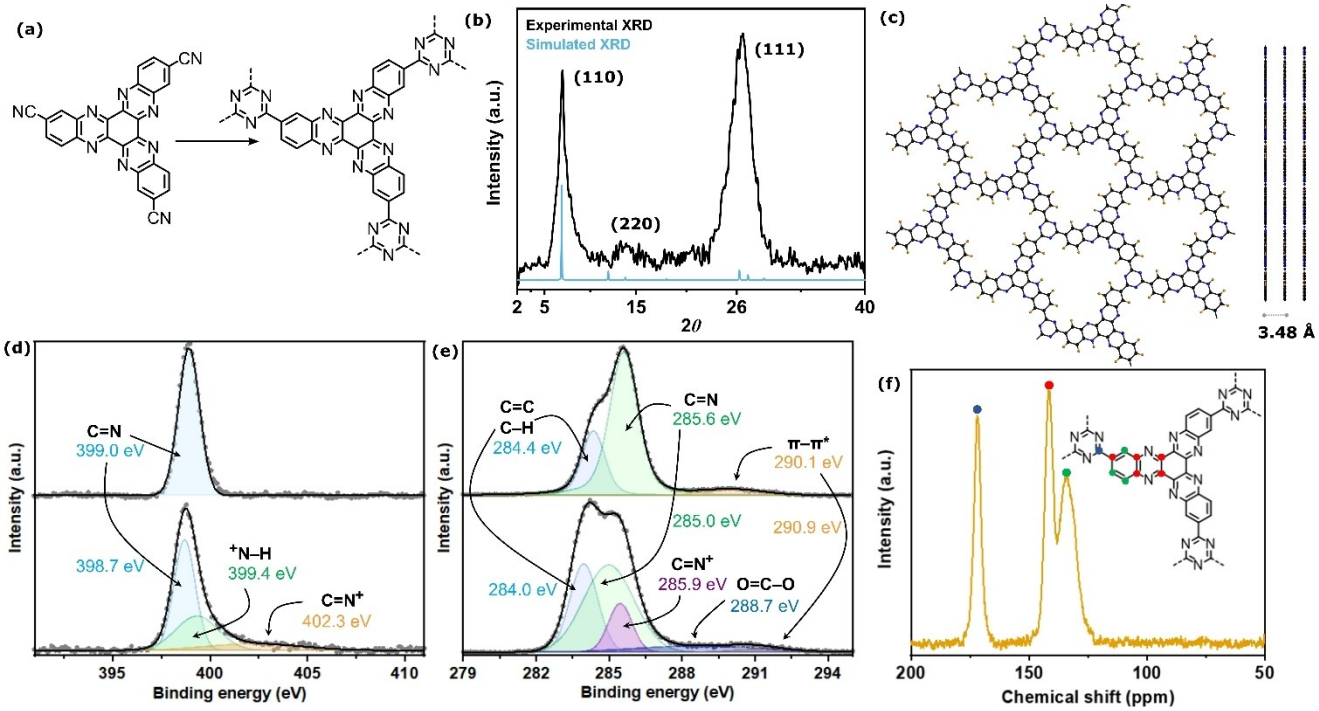

Figure 2. (a) The synthetic Scheme for HATN-CTF from HATN-CN_3 monomer showing the network propagation step via triazine formation. (b) powder XRD pattern of HATN-CTF superimposed to its simulated XRD. (c) DFT optimized AA-stacked model of HATN-CTF. High-resolution XPS of (d) N1s core level and (e) C1s core level for HATN-CTF (top) and HATN-CTF-H^+ (bottom). (f) Solid-state CP-MAS NMR of HATN-CTF showing signals from different carbons.

experiments at 77 K, and a typical Type-I adsorption, indicative of microporous solids, was recorded (Figure S5 in supplemental information). The steep increase in the gas adsorption at low-pressure region provided auxiliary confirmation of the microporous nature of the material. On the other hand, the absence of any hysteresis at high-pressure region suggested the non-existence of mesopores and accordingly, a surface area of 629 m^2/g was calculated. The pore size distribution pattern calculated by using quenched solid density functional theory (QSDFT) model echoed identical results. An average pore diameter of 1.5 nm was obtained for the synthesized HATN-CTF, which matches exactly with the theoretical model (Figure 2f, inset). Furthermore, the transmission electron and scanning electron microscopy images of the CTF revealed the porous particulate nature of the material (Figure S6, S7 in supplemental information).

Following the structural characterization, we prompted to analyze the photophysical and electrochemical properties of the CTF with the idea of examining the susceptibility of the material for the targeted anti-Markovnikov hydrocarboxylations, hydroamination and hydroazidations by using carboxylic acids, amines and azides respectively. At this stage, it was obligatory to consider the differences in fundamental chemical environment for these two reactions – the former occurring under an acidic condition, while the second one under an alkaline medium. We speculated that although the alkaline medium would not induce any structural change in the CTF, an overwhelming number of *N*-atoms present in the CTF along with their lone electron pairs would be markedly protonated in an acidic medium, which could lead to an in situ protonated HATN-CTF (HATN-CTF-H^+, Figure 3a). To prove this hypothesis, we dispersed the material in dichloromethane (DCM) with the aid of sonication and the CTF formed a stable dispersion within 2 min. After adding glacial acetic acid to the mixture and a further round of sonication, a subtle color change was observed. The formed dispersion remained stable for 30 min without the formation of any precipitation (Figure 3a). However, when NH_3 was added to this mixture followed by sonication, immediate precipitation was observed along with the change of the color of the mixture to dark green. In fact, within 5 min, almost all of the CTFs were precipitated as dark green solid. This observation endorsed the protonation-deprotonation aspect of the synthesized HATN-CTF in acidic and alkaline medium, respectively.

As a direct experimental proof of the acid-mediated protonation aspect of HATN-CTF, the acetic acid-treated material was further analyzed by the FTIR and was compared to the as-synthesized CTF (Figure S2 in supplemental information). A subtle shift in the –C=N stretching originating from the quinoxaline linkage was observed which

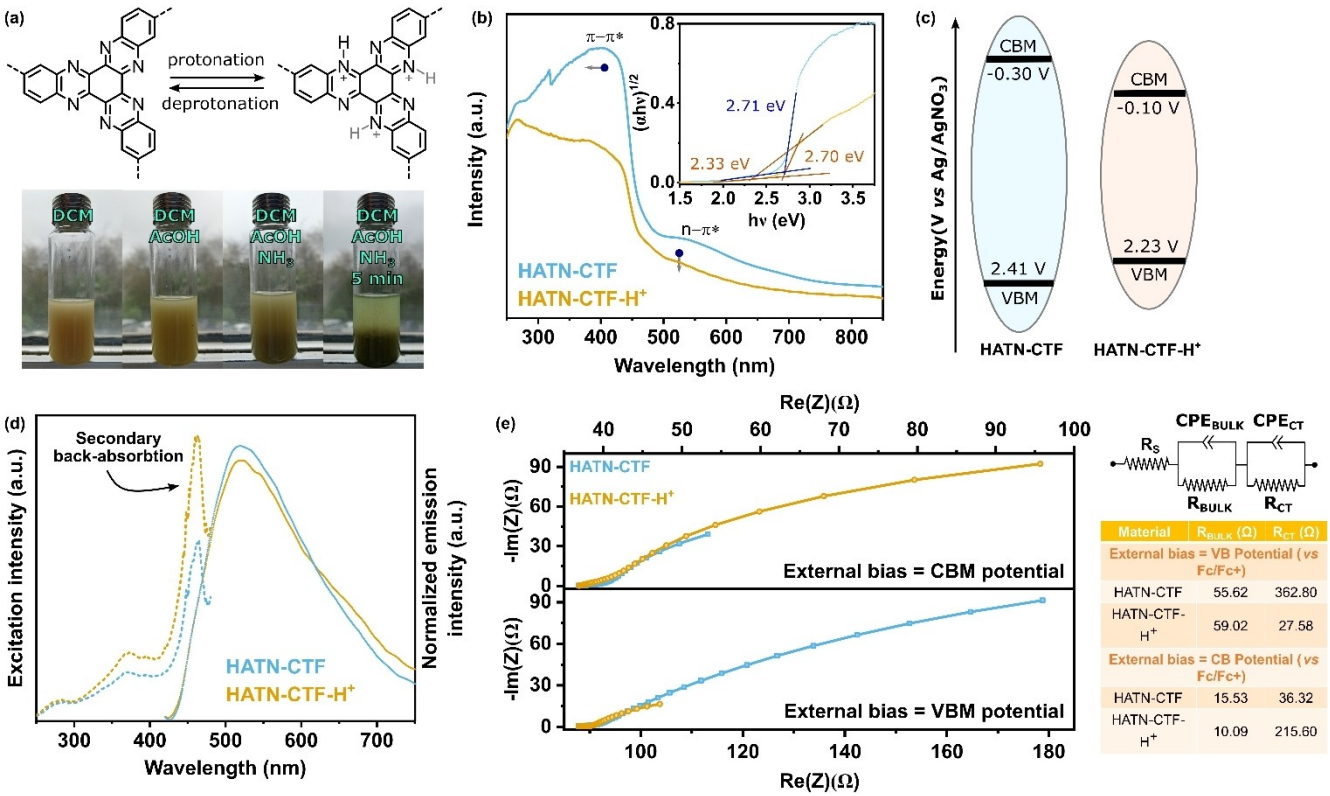

Material	R_{BULK} (Ω)	R_{CT} (Ω)
External bias = VB Potential (*vs* Fc/Fc+)		
HATN-CTF	55.62	362.80
HATN-CTF-H^+	59.02	27.58
External bias = CB Potential (*vs* Fc/Fc+)		
HATN-CTF	15.53	36.32
HATN-CTF-H^+	10.09	215.60

Figure 3. (a) The reaction scheme showing protonation-deprotonation reversibility of the HATN unit (top) and the digital images of the process (bottom). (b) Solid-state UV/Vis DRS of HATN-CTF and HATN-CTF-H^+ along with corresponding Tauc plot showing the optical band gaps of the materials (inset). (c) Schematic representation of the VB and CB potentials and band gaps of the materials. (d) The excitation (dotted line) and PL spectra of the as synthesized and the protonated CTFs (λ_{EX} 370 nm). (e) The EIS pattern of the materials under external bias potentials identical to their VB and CB potential) and corresponding equivalent Randel circuit with the numerical resistance values.

could be justified by considering their (partial) protonation. Additionally, a broad peak was observed at the 3300–3600 cm^{-1} range, possibly appearing from the superimposition of different N–H stretching overtones. XPS provided additional corroboration to this observation. As shown in Figure 2d and 2e, both C1s and N1s core level XPS manifested crucial alteration in the spectral pattern compared to the as-synthesized HATN-CTF. A noticeable decrease in the C=N peak area was recorded in HATN-CTF-H^+ together with the appearance of two new high-energy peaks, which can be ascribed to $C{=}N^+$ of the protonated sites, and carboxylate arising from the acetate counter anion of the acid. Similarly, two new high-energy peaks also appeared in the N1s XPS region, one due to the protonated N^+-H species, and the other one from $C{=}N^+$.

Furthermore, XRD analysis of HATN-CTF-H^+ revealed a subtle but important change in the diffraction pattern (Figure S8 in supplemental information). Acetic acid being a weak acid, and the pK_a of quinoxalines being higher than that of triazine, we reckoned that only the HATN units would be protonated. However, assessing the absolute extent of protonation was non-trivial. Therefore, we considered systematic and successive protonation of the HATN units in the CTF and modeled corresponding theoretical structures. Three successive models were developed, HATN-CTF-1H, –2H, and –3H, where each HATN was protonated with one acid, two acids, and three acids respectively (Figure S9–S12 in supplemental information). As the HATN units remained protonated, the acetate counter anions occupied the CTF interplanar space and thereby increased the *c/a* ratio of the crystal lattices. This increase in interplanar distance was reflected on the XRD, where the (110) peak shifted more towards a low Bragg angle (Figure S8 in supplemental information). The XRD pattern simulated from the HATN-CTF-2H and HATN-CTF-3H showed good agreement with the experimentally obtained XRD of HATN-CTF-H^+ (Figure S13 in supplemental information), further confirming our protonation theory. Moreover, as the interlayer distance of CTF planes increased, their exfoliation would also become more feasible. This can explain our initial observation of the stable dispersion of HATN-CTF-H^+ in DCM obtained by simple sonication (Figure 2a).

Recently, Thomas *et al.* have substantiated that protonation could drastically change the photophysical and electrochemical properties of organic networks, i.e., the valence and conduction band potentials, *ergo* the band gaps.[34, 98] Therefore, we found it instrumental to investigate the photo-electrochemical properties of HATN-CTF-H^+ in parallel to the parent CTF to assess the entire catalytic scenery. The solid-state diffuse reflectance UV/Vis spectrum (DRS) of HATN-CTF exhibited a steep band with an absorption maximum at 400 nm wavelength, which could be assigned to the typical π–π* transition (Figure 3b). An auxiliary small absorption peak with a maximum at 520 nm was observed as well, originating from the n-π* absorption in the material. After protonation, the π–π* band manifested a small 10 nm blueshift whereas the n-π* absorption band mostly disappeared. This could be due to the lack of electron lone pairs in the protonated CTF. Accordingly, an optical band gap of 2.71 eV was calculated for HATN-CTF from the corresponding Tauc plot (Figure 3b, inset). On the other hand, the Tauc plot of HATN-CTF-H^+ revealed the existence of two energy gaps, 2.70 eV and 2.33 eV. The low energy gap indeed indicated the protonation-induced band gap lowering, which has been corroborated by other groups as well.[64–65] The higher energy one, being similar to that of the unprotonated CTF, was ascribed to the band states similar to that of the parent HATN-CTF.

Mott–Schottky analyses of the CTFs were conducted to obtain flat-band potentials of −0.3 V and −0.1 V (*vs* Ag/$AgNO_3$) for HATN-CTF and HATN-CTF-H^+ respectively (with ferrocene as an external standard), which can be well-approximated as corresponding conduction band (CB) minimum potentials. Accordingly, valence band (VB) maximum potentials of +2.41 V *vs* Ag/$AgNO_3$ (+2.37 V vs SCE) and 2.23 V *vs* Ag/$AgNO_3$ (+2.19 V *vs* SCE) were calculated for HATN-CTF and HATN-CTF-H^+ respectively (Figure 3c and Figure S14 in supplemental information). The theoretically computed highest occupied and lowest unoccupied molecular orbitals (HOMO–LUMO) for HATN-CTF revealed that both were localized on the HATN moiety (Figure S15, S16 in supplemental information). Protonation of this unit was expected to change MO potentials, *ergo* altering the energy gaps. For a better justification, we further calculated the HOMO–LUMO, HOMO-1/LUMO + 1, and HOMO-2/LUMO + 2 for the DFT-optimized molecular HATN and its various protonated analogs. The results revealed that with each protonation, the energy gap indeed decreased (Figure S17 in supplemental information). Moreover, the HOMO-1 and HOMO-2 became closer in energy to the HOMO eventually forming degenerate levels for the *tris*-protonated HATN. An identical observation was noted for the LUMO as well. These results not only shed light on the origin of the decreased energy gap of HATN-CTF post-protonation but also justified the existence of more than one closely lying energy gap (refer to the Tauc plot).

The solid-state photoluminescence (PL) spectroscopic analysis of the materials also indicated subtle but significant differences. The luminescence intensity (normalized against maximum excitation intensity) of HATN-CTF decreased by ca. 5% after protonation, whereas the PL tail became slightly broader (Figure 3d). As protonation did not induce any structural dissolution of HATN-CTF to create any new defect sites, these PL results insinuated that the radiative recombination of the electron-hole pairs was relatively more suppressed after the protonation. The solid-state time-resolved PL analysis provided additional corroboration to this observation. Both the protonated and pristine CTF featured decay time on microsecond scale, inferring the highly suppressed electron-hole recombination in the materials (Figure S18 in supplemental information). While both decay patterns were fitted by a two-exponential function, HATN-CTF–H+ showed an enhanced lifetime of 1.62 μs compared to 1.32 μs of the pristine HATN-CTF. In line with this, the photocurrent measurement of the materials also revealed that after protonation, the photocurrent response

of the CTF increased and the decay became slower than the pristine material (Figure S19 in SI). Moreover, the excitation spectra revealed a strong back-absorption with a maximum at 462 nm for both materials, owing to the low Stokes shift (Figure 3d). This was envisaged to be highly beneficial from a photocatalysis perspective as such back-absorption of the self-emitted photons would inevitably augment the quantum efficiency of the material during catalysis. Additionally, the impedance spectra of the materials calculated at VB and CB external bias potentials provided further insights into the charge transfer dynamics in the material during targeted catalysis. The impedance spectra of the materials under both oxidative and reductive bias can be represented by the same equivalent Randel circuit, $R_S + [CPE_{BULK}/R_{BULK}] + [CPE_{CT}/R_{CT}]$, where R_{BULK} represented the resistance of the bulk material and R_{CT} indicated the charge transfer resistance from the material to the medium (Figure 3e). Under either VB or CB bias, both materials manifested similar R_{BULK}, whereas the R_{CT} significantly dropped for HATN-CTF–H+ under oxidative conditions, and for HATN-CTF under reductive conditions (Figure 3e, inset table). A physical interpretation of these numerical results would be that the material would perform a photooxidation reaction well under acidic conditions whereas a photoreduction under alkaline conditions.

With the knowledge of the photophysical and electrochemical properties of the HATN-CTF and its protonated analogs, the synthesized material was employed as a heterogeneous photocatalyst for the anti-Markovnikov addition reaction of carboxylic acid to alkenes via a single-electron-transfer (SET) pathway. For that, *trans*-anethole (**1a**) and benzoic acid (**2a**) were chosen as the model substrates in the search for optimal reaction conditions (Table S1 in supplemental information). In particular, when the mixture of HATN-CTF (5 mg), *trans*-anethole (**1a**), and benzoic acid (**2a**) in dichloromethane was irradiated at 390 nm light in presence of *p*-tolyl disulfide (**3a**) as a hydrogen-atom-transfer (HAT) catalyst, the desired product (**4a**) was obtained in 85 % yield at room temperature after 24 h of reaction (Table S1, entry 1 in supplemental information). To improve the outcome further, other HATs were investigated and among them, the use of electron-rich disulfide (**3b**) only yielded 25 % of **4a** after 24 h (Table S1, entry 2 in supplemental information). However, to our surprise, replacing the aromatic disulfide with an aliphatic disulfide (**3c**) completely failed to provide **4a** (Table S1, entry 3 in supplemental information).

Other classes of HATs such as aromatic thiols were also examined in the reaction, however, both electron-rich and deficient thiols (**3d** and **3e**) could not prove to be more proficient than **3a** (Table S1, entries 4–5 in supplemental information). Furthermore, different polar solvents were applied in the reaction: while MeCN provided 48 % of **4a**, DMSO failed to promote the reaction (Table S1, entries 6–7 in supplemental information). Delighted by these results, control experiments were also conducted to confirm the role of each reagent under the optimized reaction conditions. As expected, a blank experiment without the presence of HATN-CTF, resulted in only 8 % yield of **4a** (Table S1, entry 8 in supplemental information). Similarly, when the reaction was performed in the absence of HAT (**3a**) or light, no formation of the product was detected (Table S1, entries 9–10 in supplemental information). Moreover, the use of the monomer of the newly synthesized HATN-CN_3 as a photocatalyst, only led to a 32 % yield of **4a**, indicating that the high ordered 2D skeletons, π-conjugation, crystalline structure as well as the porosity of the CTF facilitated the enhanced photocatalysis property to facile this reaction (Table S1, entry 11 in supplemental information).

After achieving the optimized conditions in our hand, we moved to assess the substrate scope of the hydrocarboxylation reaction (Figure 4). Diverse benzoic acid derivatives such as electron-rich (–OMe), and electron-deficient (–F) groups at different substitution positions, reacted quite well under our photocatalytic conditions and provided the corresponding products in good to excellent yield (**4a–c**; 38–85 % yield). Furthermore, the heteroaromatic carboxylic acid e.g., thiophene-2-carboxylic acid was also suitable in this reaction (**4d**; 77 % yield). Inspired by this, we turned to investigate the scope of the aliphatic carboxylic acids to reveal the wide generality of our protocol. Acetic acid, propanoic acid, isobutyric acid as well as cyclohexyl carboxylic acid were able to afford the desired products in good to excellent yields (**4e–4h**; 49–88 % yield). Furthermore, when levulinic acid was added to the reaction, **4i** was procured in 81 % yield. Interestingly, Boc-gly-OH was also applicable in our methodology and provided the selective hydrocarboxylation product (**4j**, 36 % yield) over the hydroamination product. We argued that it could be due to the faster deprotonation of carboxylic acid by the HAT which led to a higher concentration of the nucleophilic carboxylate anion. Other cyclic aliphatic carboxylic acids such as cyclopropanoic acid and tetrahydrofuran-2-carboxylic acid were also transformed into the corresponding hydrocarboxylated products (**4k**, 57 % yield & **4l**, 43 % yield, 1:1 d.r.) respectively. Remarkably, the inclusion of acrylic acid in the reaction resulted exclusively in the hydrocarboxylation product **4m** (62 % yield). In this case, no cyclization process occurred following the nucleophilic addition of acrylic acid to the radical cation.

Furthermore, the effect of different alkenes was also investigated by using acetic acid as the model coupling partner, and under our reaction conditions, in addition to trans-anethole moiety, trans-stilbene was well acceptable to provide 80 % yield of the product (**4n**). Additionally, the change of electronic as well as the substitution pattern in trans-stilbene did not influence the formation of the hydrocarboxylated products to a great extent. The reaction with *p*-Me, –Cl, and –F-substituted stilbenes produced the corresponding ester products (**4o–4q**) in excellent yields (69–86 %) with the mixture of regioisomers. *m*-Br and –CN-substituted stilbenes were further explored in our reaction and displayed moderate to high yields (**4r–4s**; 56–81 %). To our surprise, the addition of triacetyl resveratrol in the reaction afforded the corresponding ester (**4t**) in 78 % yield (with 1.87:1 r.r. of regioisomeric ratio).

To show the application of our method, late-stage functionalization (LSF) of the bioactive/drugs was carried

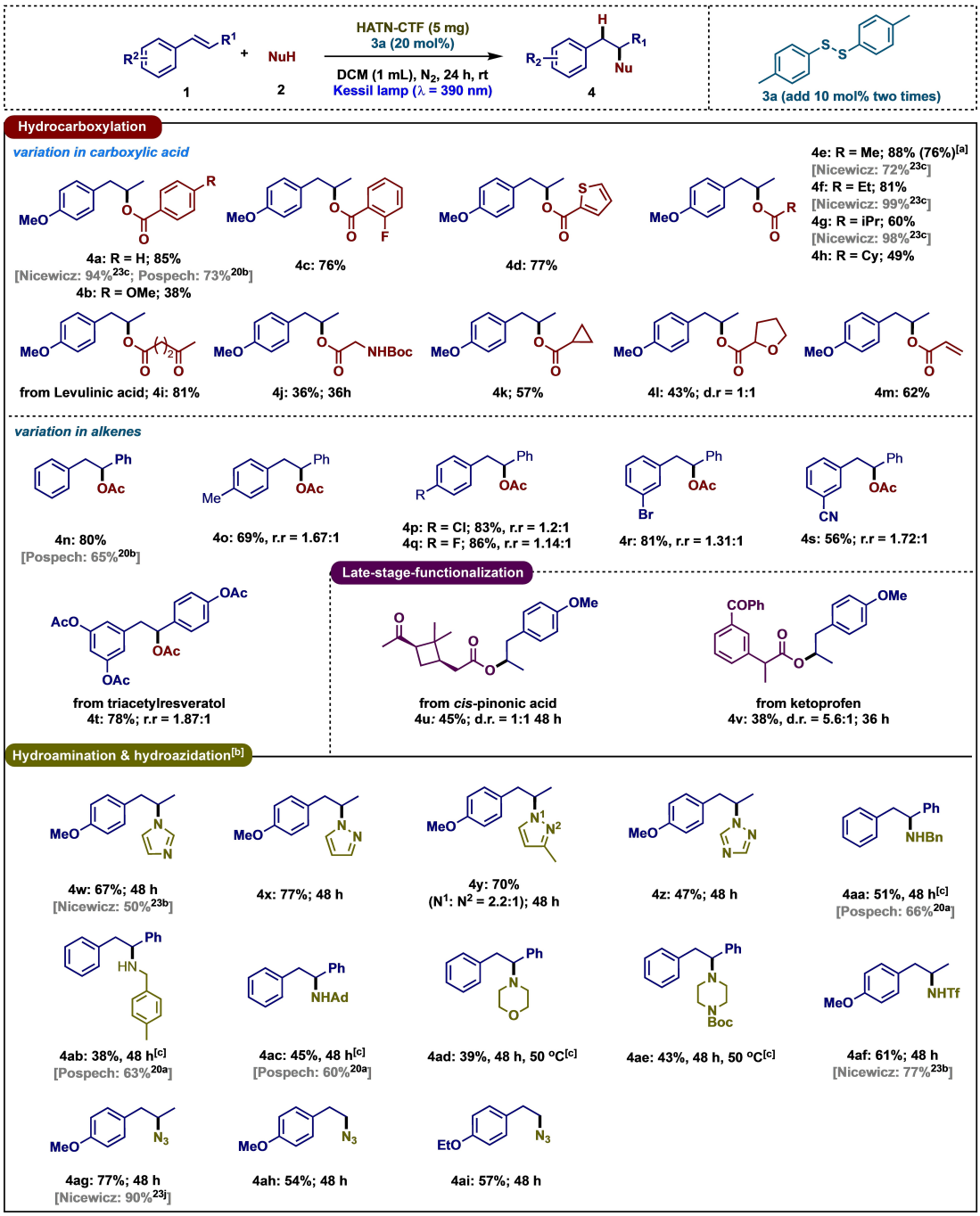

Figure 4. Substrates scope for the hydro-functionalization reactions. [a,b] Reaction conditions: as mentioned in Table S1 entry 1. Reaction was conducted for 24 h until otherwise mentioned. [a] 10 mmol scale reaction. [b] DCM : TFE (7 : 3) was used instead of DCM. [c] DCM as a solvent was used. Previous results using homogeneous photocatalysts are shown in parentheses.

out (Figure 4) and for this purpose, cis-pinonic acid (bioactive) and ketoprofen (NSAID drug) were employed in the catalytic reaction to obtain the corresponding products (**4u** and **4v**) in 45 % and 38 % yield respectively. To further establish the application of the protocol, we conducted a gram-scale synthesis of **4e** by using 10 mmol of *trans-anethole* (cf. Figure S20 in supplemental information SI), and to our delight, 76 % yield of the desired product was recorded. The recyclability of this material was also assessed against the same reaction and the catalytic activity (measured as product yield per 10 mg of CTF photocatalyst after 6 h at ca. 50 % conversion) of the successive runs are compared. HATN-CTF maintained its reactivity for up to 6 repetitive catalytic cycles without any significant drop in the catalytic activity (Figure S21 in supplemental information). The reused catalyst analyzed by XRD after the 6th catalytic run showed a similar diffraction pattern to HATN-CTF-H$^+$ (Figure S22 in supplemental information). The C1s and N1s

core level XPS of reused HATN-CTF also showed a comparable spectral pattern as HATN-CTF-H^+ (Figure S23 in supplemental information). Moreover, the FTIR analysis of the reused catalyst also provided similar peaks as HATN-CTF-H^+, showing that the material retained its chemical structure after photocatalysis (Figure S24 in supplemental information). To prove the heterogeneous nature of the catalysis, two parallel filtration tests were performed (cf. Supporting Information for details). When the catalyst was filtered off after 4 h of irradiation under standard catalytic condition, no new product formation can be observed. On the other hand, filtering off the catalyst from DCM after 12 h of photo-irradiation followed by standard amounts of substrate addition failed to produce any product. These results confirmed the heterogeneous nature of the catalysis and further endorsed the structural integrity of HATN-CTF under reaction conditions.

In addition to the hydrocarboxylation, hydroamination and hydroazidation reaction of alkene were also accomplished using HATN-CTF. In this case, imidazole was used as the model amine source to react with *trans*-anethole (**1a**). When the reaction was executed under the previously optimized reaction conditions (Table S1, entry 1 in supplemental information), only 52 % of the hydroaminated product (**4w**) was detected after 48 h of irradiation. In this context, we must mention that previously the acidic proton of the carboxylic acid played a crucial role in the efficient catalysis of the HATN-CTF. As established before, through protonation, the redox potential of HATN-CTF was altered and decreased its charge transfer resistance which facilitated the hydrocarboxylation reaction. Therefore, we envisioned that a solvent with an acidic nature (able to form H-bond) could assist immensely in speeding up the reaction. With this conviction, several solvents with potential H-bond forming capabilities were examined in the reaction and it was found that trifluoroethanol (TFE), a classical H-bond donor solvent, indeed boosted the reaction, providing **4w** in 67 % yield. With these newly optimized conditions, several hydroaminated products, **4x** (77 % yield), **4y** (70 % yield), and **4z** (47 % yield) were obtained in moderate to excellent yields by using pyrazole, 3-methyl pyrazole, and triazole as the amine source. Expediently, our method is also applicable to primary and secondary amines. Benzyl amine, *p*-methyl benzylamine, 1-adamantyl amines, morpholine, and boc-piperazine could be coupled with trans-stilbene in anti-Markovnikov manner using our protocol, affording the corresponding amines in moderate to good yields (**4aa**–**4ae**; 38–51 %). Primary sulfonamide ($TfNH_2$) as well as trimethylsilyl azide ($TMSN_3$) also responded excellently in our reaction, providing the desired products (**4af** in 61 % yield and **4ag** in 77 % yield). Furthermore, terminal alkenes can be employed in our system to obtain the hydroazidation products in good yields (**4ah**–**4ai**; 38–51 %).

Inspired by these catalytic activities, we became interested in investigating the reaction mechanism of this reaction (Figure 5). In the beginning, the radical quenching experiment with TEMPO did not afford any product formation, which clearly suggested a radical pathway (Figure 5a). In fact, we detected the TEMPO-anethole adduct via HRMS analysis. Further quenching experiment with $CuCl_2$ indicated that a single-electron transfer was taking place since no product was detected (Figure 5a). Addition-

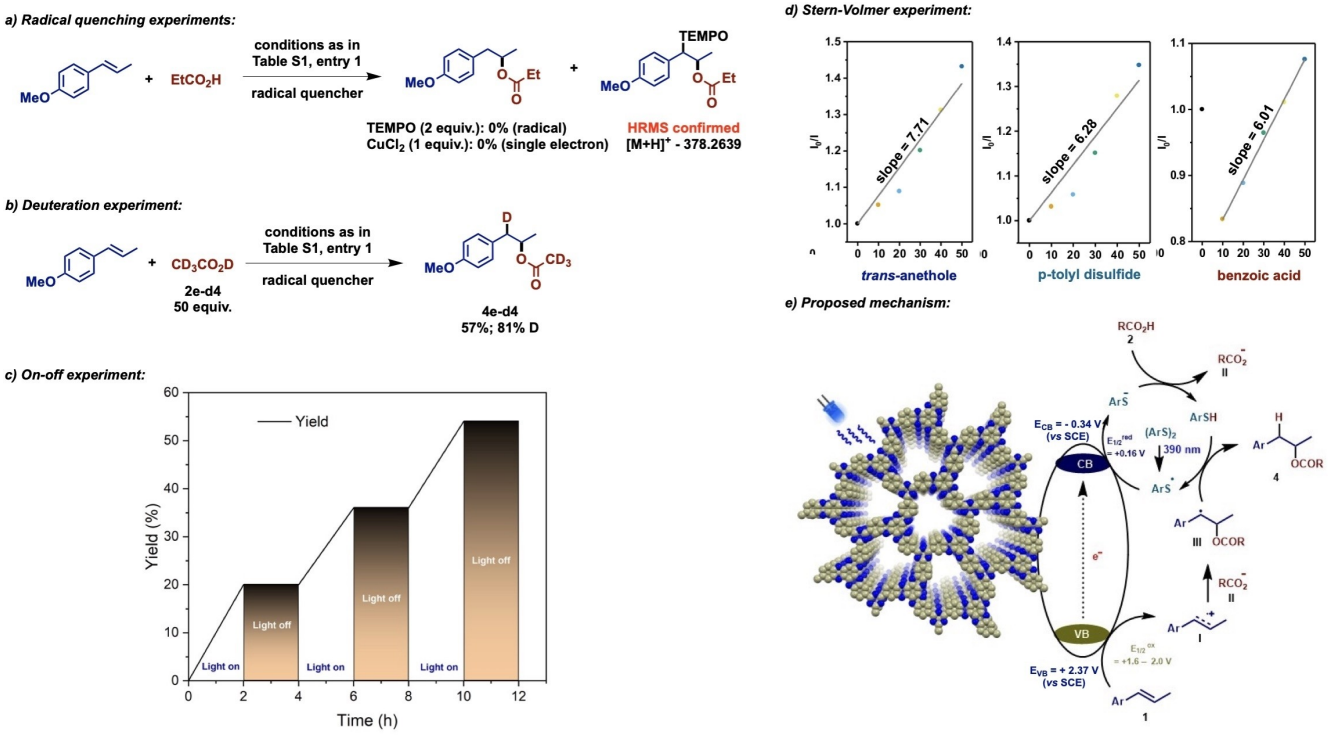

Figure 5. Mechanistic studies and proposed mechanism for hydro-carboxylation.

ally, the deuteration experiment confirmed that the acidic proton was abstracted by the HAT (*p*-tolyl disulfide) and transferred to the β-position of the styrene derivatives (Figure 5b). Furthermore, it was proven from the on-off experiments that the material HATN-CTF acted as a photocatalyst rather than a photosensitizer (Figure 5c). We also performed Stern–Volmer in our reaction and it was found that the styrene derivative had the highest affinity to quench the excited state of the HATN-CTF (Figure 5d). Based on these results, we have proposed a possible mechanism (Figure 5e). At first, irradiation by the light created a charge separation and formed an electron-hole pair in HATN-CTF. This was also evident from the in situ EPR measurements of the solid sample (Figure S23 in supplemental information) which showed enhancement of the EPR signal intensity during irradiation of the catalysts. Next, the styrene (**1**) was oxidized by the VB of the material, generating the corresponding radical cation (**I**). This enhanced the charge separation process and increased the EPR signal intensity of the photoexcited CB electrons (blue lines in Figure S25 in supplemental information). The oxidation of styrene by the hole and formation of radical cation were confirmed by trapping the in situ formed radical with 5,5-dimethyl-1-pyrrolin N-oxide (DMPO) to form DMPO-radical spin adducts, the nature of these adducts is unclear due to the not well resolved hyperfine structure (partially resolved in the 2nd derivative spectrum, inset in Figure S26 in supplemental information) and superimposed its signal with the CB signal (Figure S26 in supplemental information).

In the meantime, the irradiated light assisted in breaking down the aryl disulfide into ArS$^{\bullet}$ which was immediately reduced to the corresponding anion (ArS^{-}) by the CB of the HATN-CTF. The sulfide anion (ArS^{-}) was responsible to abstract the acidic proton from the carboxylic acid, resulting in thiol (ArSH) and carboxylate intermediate (**II**) which intercepted this radical cation (**I**) in our reaction to generate the intermediate **III**. In the end, this intermediate (**III**) was converted into the product (**4**) via a hydrogen radical transfer from ArSH, leading to generate ArS$^{\cdot}$ for the next HAT cycle. As the in situ protonation of HATN-CTF has been established, we hypothesized that during photocatalytic hydrocarboxylation, the CTF would be protonated to HATN-CTF-H^{+}. This protonated CTF would then catalyze the reaction following the abovementioned mechanism. To this end, we also considered the possibility of the acid species functioning as sacrificial agents during photocatalysis. As direct oxidation and/or reduction of carboxylic acids ought to generate CO_2 (via oxidative decarboxylation) and H_2 (via proton reduction), we checked for the presence of these gases in the catalytic reactor headspace after 12 h of reaction. Neither of the two gases can be detected on the gas chromatogram, while only peaks for air were found (Figure S27 in supplemental information), which indicated that the acid species only served as the catalytic substrate and not as a sacrificial agent. Moreover, the excitation and emission spectra of a set of HATN-CTF dispersions in DCM independently titrated with varying concentrations of acetic acid showed that with increasing acid concentration the normalized steady-state PL intensity gradually quenched (Figure S28a in supplemental information), whereas the time-resolved PL confirmed a successively increased lifetime of the separated charge carriers (Figure S28c in supplemental information). These observations further inferred the important role of acid-mediated in situ protonation in the suppression of charge carriers. Additionally, the excitation pattern of the dispersion also changed with increasing acid concentration along with a gradual blue shift of the excitation maxima, which can be correlated to the gradual change in the CTF backbone via protonation (Figure S28b in supplemental information). Indeed, it can also explain the protonated form of the recycled HATN-CTF discussed earlier. On the other hand, during hydroamination, i.e., alkaline catalytic condition, HATN-CTF would remain in its parent deprotonated form and follow a similar reaction mechanism as that of hydrocarboxylation, where the amine moiety would function as the nucleophile.

Conclusions

In conclusion, a HATN-based CTF network has been developed as a super-oxidizing and inexpensive heterogeneous photocatalyst for the anti-Markovnikov hydrofunctionalizations of styrenes. The high valence band potential of the CTF made it susceptible to catalyze both electron-donating as well as withdrawing substrates. Moreover, the solvent medium-induced in situ protonation of the CTF, the changes in its photophysical and electrochemical properties triggered by this chemical change, and its impact on the catalytic propensity of the material were assessed. Tuning of the catalytic conditions based on this knowledge allowed our protocols to furnish the desired regioselective C–N and C–O coupled products in good to excellent yields. Further modifications in the skeleton of our CTF is undergoing to achieve higher oxidation potential for the direct functionalization in the aromatic rings.

Supporting Information

Supporting Information is available from the Wiley Online Library or from the author.

Acknowledgements

SD thanks the FWO research project grant as well as the Odysseus grant from FWO. RM thanks the BOF fellowship and Marie Curie postdoctoral fellowship (Project id: 101108702) for the financial assistance to finish this work. PVDV, JC and IN acknowledge the FWO-Vlaanderen for research grant G020521 N. PVDV acknowledges the research board of UGent (BOF) through a Concerted Research Action (GOA010-17, 01GB1017 and 01G01017). J.C. acknowledge the financial support from UGent (BOF.PDO. 2022.0032.01). All authors thank UGent NMR Core Facility for the solid-state NMR measurements. Open Access funding enabled and organized by Projekt DEAL.

Conflict of Interest

The authors declare no conflict of interest.

Data Availability Statement

The data that support the findings of this study are available on request from the corresponding author. The data are not publicly available due to privacy or ethical restrictions.

Keywords: Covalent triazine frameworks · Heterogeneous Photocatalysis · Hydrocarboxylation · Hydroamination · hydroazidation

[1] H. Wang, H. Wang, Z. Wang, L. Tang, G. Zeng, P. Xu, M. Chen, T. Xiong, C. Zhou, X. Li, D. Huang, Y. Zhu, Z. Wang, J. Tang, *Chem. Soc. Rev.* **2020**, *49*, 4135–4165.
[2] A. López-Magano, S. Daliran, A. R. Oveisi, R. Mas-Ballesté, A. Dhakshinamoorthy, J. Alemán, H. Garcia, R. Luque, *Adv. Mater.* **2023**, *35*, 2209475.
[3] A. G. Slater, A. I. Cooper, *Science* **2015**, *348*, aaa8075.
[4] P. She, Y. Qin, X. Wang, Q. Zhang, *Adv. Mater.* **2022**, *34*, 2101175.
[5] A. P. Côté, A. I. Benin, N. W. Ockwig, M. O'Keeffe, A. J. Matzger, O. M. Yaghi, *Science* **2005**, *310*, 1166–1170.
[6] H. M. El-Kaderi, J. R. Hunt, J. L. Mendoza-Cortés, A. P. Côté, R. E. Taylor, M. O'Keeffe, O. M. Yaghi, *Science* **2007**, *316*, 268–272.
[7] M. Traxler, S. Gisbertz, P. Pachfule, J. Schmidt, J. Roeser, S. Reischauer, J. Rabeah, B. Pieber, A. Thomas, *Angew. Chem. Int. Ed.* **2022**, *61*, e202117738.
[8] P. T. Parvatkar, S. Kandambeth, A. C. Shaikh, I. Nadinov, J. Yin, V. S. Kale, G. Healing, A.-H. Emwas, O. Shekhah, H. N. Alshareef, O. F. Mohammed, M. Eddaoudi, *J. Am. Chem. Soc.* **2023**, *145*, 5074–5082.
[9] A. Basak, S. Karak, R. Banerjee, *J. Am. Chem. Soc.* **2023**, *145*, 7592–7599.
[10] R. Chen, J.-L. Shi, Y. Ma, G. Lin, X. Lang, C. Wang, *Angew. Chem. Int. Ed.* **2019**, *58*, 6430–6434.
[11] J.-L. Shi, R. Chen, H. Hao, C. Wang, X. Lang, *Angew. Chem. Int. Ed.* **2020**, *59*, 9088–9093.
[12] P.-F. Wei, M.-Z. Qi, Z.-P. Wang, S.-Y. Ding, W. Yu, Q. Liu, L.-K. Wang, H.-Z. Wang, W.-K. An, W. Wang, *J. Am. Chem. Soc.* **2018**, *140*, 4623–4631.
[13] N. Kang, J. H. Park, K. C. Ko, J. Chun, E. Kim, H.-W. Shin, S. M. Lee, H. J. Kim, T. K. Ahn, J. Y. Lee, S. U. Son, *Angew. Chem. Int. Ed.* **2013**, *52*, 6228–6232.
[14] Y. Meng, Y. Luo, J.-L. Shi, H. Ding, X. Lang, W. Chen, A. Zheng, J. Sun, C. Wang, *Angew. Chem. Int. Ed.* **2020**, *59*, 3624–3629.
[15] Y. Qian, D. Li, Y. Han, H.-L. Jiang, *J. Am. Chem. Soc.* **2020**, *142*, 20763–20771.
[16] X. Kan, J.-C. Wang, Z. Chen, J.-Q. Du, J.-L. Kan, W.-Y. Li, Y.-B. Dong, *J. Am. Chem. Soc.* **2022**, *144*, 6681–6686.
[17] H.-S. Lu, W.-K. Han, X. Yan, C.-J. Chen, T. Niu, Z.-G. Gu, *Angew. Chem. Int. Ed.* **2021**, *60*, 17881–17886.
[18] F. Jin, E. Lin, T. Wang, D. Yan, Y. Yang, Y. Chen, P. Cheng, Z. Zhang, *Chem* **2022**, *8*, 3064–3080.
[19] V. S. Vyas, F. Haase, L. Stegbauer, G. Savasci, F. Podjaski, C. Ochsenfeld, B. V. Lotsch, *Nat. Commun.* **2015**, *6*, 8508.
[20] S. Lin, C. S. Diercks, Y.-B. Zhang, N. Kornienko, E. M. Nichols, Y. Zhao, A. R. Paris, D. Kim, P. Yang, O. M. Yaghi, C. J. Chang, *Science* **2015**, *349*, 1208–1213.
[21] J.-R. Wang, K. Song, T.-X. Luan, K. Cheng, Q. Wang, Y. Wang, W. W. Yu, P.-Z. Li, Y. Zhao, *Nat. Commun.* **2024**, *15*, 1267.
[22] C. G. Gruber, L. Frey, R. Guntermann, D. D. Medina, E. Cortés, *Nature* **2024**, https://doi.org:10.1038/s41586-024–07483-0.
[23] W. Zhang, L. Chen, S. Dai, C. Zhao, C. Ma, L. Wei, M. Zhu, S. Y. Chong, H. Yang, L. Liu, Y. Bai, M. Yu, Y. Xu, X.-W. Zhu, Q. Zhu, S. An, R. S. Sprick, M. A. Little, X. Wu, S. Jiang, Y. Wu, Y.-B. Zhang, H. Tian, W.-H. Zhu, A. I. Cooper, *Nature* **2022**, *604*, 72–79.
[24] F. Auras, L. Ascherl, V. Bon, S. M. Vornholt, S. Krause, M. Döblinger, D. Bessinger, S. Reuter, K. W. Chapman, S. Kaskel, R. H. Friend, T. Bein, *Nat. Chem.* **2024**, https://doi.org:10.1038/s41557-024–01527-8.
[25] E. Hamzehpoor, C. Ruchlin, Y. Tao, C.-H. Liu, H. M. Titi, D. F. Perepichka, *Nat. Chem.* **2023**, *15*, 83–90.
[26] H. Hu, Z. Wang, L. Cao, L. Zeng, C. Zhang, W. Lin, C. Wang, *Nat. Chem.* **2021**, *13*, 358–366.
[27] M. Calik, F. Auras, L. M. Salonen, K. Bader, I. Grill, M. Handloser, D. D. Medina, M. Dogru, F. Löbermann, D. Trauner, A. Hartschuh, T. Bein, *J. Am. Chem. Soc.* **2014**, *136*, 17802–17807.
[28] X. Wang, L. Chen, S. Y. Chong, M. A. Little, Y. Wu, W.-H. Zhu, R. Clowes, Y. Yan, M. A. Zwijnenburg, R. S. Sprick, A. I. Cooper, *Nat. Chem.* **2018**, *10*, 1180–1189.
[29] X. Wang, K. Maeda, A. Thomas, K. Takanabe, G. Xin, J. M. Carlsson, K. Domen, M. Antonietti, *Nat. Mater.* **2009**, *8*, 76–80.
[30] R. Liu, Y. Chen, H. Yu, M. Položij, Y. Guo, T. C. Sum, T. Heine, D. Jiang, *Nat. Catal.* **2024**, *7*, 195–206.
[31] R. Chen, Y. Wang, Y. Ma, A. Mal, X.-Y. Gao, L. Gao, L. Qiao, X.-B. Li, L.-Z. Wu, C. Wang, *Nat. Commun.* **2021**, *12*, 1354.
[32] X. Guan, H. Li, Y. Ma, M. Xue, Q. Fang, Y. Yan, V. Valtchev, S. Qiu, *Nat. Chem.* **2019**, *11*, 587–594.
[33] P. Das, G. Chakraborty, J. Roeser, S. Vogl, J. Rabeah, A. Thomas, *J. Am. Chem. Soc.* **2023**, *145*, 2975–2984.
[34] J. Yang, S. Ghosh, J. Roeser, A. Acharjya, C. Penschke, Y. Tsutsui, J. Rabeah, T. Wang, S. Y. Djoko Tameu, M.-Y. Ye, J. Grüneberg, S. Li, C. Li, R. Schomäcker, R. Van De Krol, S. Seki, P. Saalfrank, A. Thomas, *Nat. Commun.* **2022**, *13*, 6317.
[35] M. Liu, L. Guo, S. Jin, B. Tan, *J. Mater. Chem. A* **2019**, *7*, 5153–5172.
[36] C. Krishnaraj, H. S. Jena, K. Leus, P. Van Der Voort, *Green Chem.* **2020**, *22*, 1038–1071.
[37] S. Abednatanzi, P. Gohari Derakhshandeh, K. Leus, H. Vrielinck, F. Callens, J. Schmidt, A. Savateev, P. Van Der Voort, *Sci. Adv.* **2020**, *6*, eaaz2310.
[38] H. S. Jena, C. Krishnaraj, S. Parwaiz, F. Lecoeuvre, J. Schmidt, D. Pradhan, P. Van Der Voort, *ACS Appl. Mater. Interfaces* **2020**, *12*, 44689–44699.
[39] Y. Zou, S. Abednatanzi, P. Gohari Derakhshandeh, S. Mazzanti, C. M. Schüßlbauer, D. Cruz, P. Van Der Voort, J.-W. Shi, M. Antonietti, D. M. Guldi, A. Savateev, *Nat. Commun.* **2022**, *13*, 2171.
[40] S. Vijayakrishnan, J. W. Ward, A. I. Cooper, *ACS Catal.* **2022**, *12*, 10057–10064.
[41] K. Sun, O. J. Silveira, Y. Ma, Y. Hasegawa, M. Matsumoto, S. Kera, O. Krejčí, A. S. Foster, S. Kawai, *Nat. Chem.* **2023**, *15*, 136–142.
[42] W. Zhao, P. Yan, H. Yang, M. Bahri, A. M. James, H. Chen, L. Liu, B. Li, Z. Pang, R. Clowes, N. D. Browning, J. W. Ward, Y. Wu, A. I. Cooper, *Nat. Synth.* **2022**, *1*, 87–95.
[43] M. Bhadra, S. Kandambeth, M. K. Sahoo, M. Addicoat, E. Balaraman, R. Banerjee, *J. Am. Chem. Soc.* **2019**, *141*, 6152–6156.

[44] W. Huang, J. Byun, I. Rörich, C. Ramanan, P. W. M. Blom, H. Lu, D. Wang, L. Caire da Silva, R. Li, L. Wang, K. Landfester, K. A. I. Zhang, *Angew. Chem. Int. Ed.* **2018**, *57*, 8316–8320.
[45] W. Huang, N. Huber, S. Jiang, K. Landfester, K. A. I. Zhang, *Angew. Chem. Int. Ed.* **2020**, *59*, 18368–18373.
[46] S. Bi, Z. Zhang, F. Meng, D. Wu, J.-S. Chen, F. Zhang, *Angew. Chem. Int. Ed.* **2022**, *61*, e202111627.
[47] W. Huang, B. C. Ma, H. Lu, R. Li, L. Wang, K. Landfester, K. A. I. Zhang, *ACS Catal.* **2017**, *7*, 5438–5442.
[48] X. Lan, X. Liu, Y. Zhang, Q. Li, J. Wang, Q. Zhang, G. Bai, *ACS Catal.* **2021**, *11*, 7429–7441.
[49] C. B. Meier, R. Clowes, E. Berardo, K. E. Jelfs, M. A. Zwijnenburg, R. S. Sprick, A. I. Cooper, *Chem. Mater.* **2019**, *31*, 8830–8838.
[50] Z.-A. Lan, Y. Fang, Y. Zhang, X. Wang, *Angew. Chem. Int. Ed.* **2018**, *57*, 470–474.
[51] W. Huang, Q. He, Y. Hu, Y. Li, *Angew. Chem. Int. Ed.* **2019**, *58*, 8676–8680.
[52] C. Yang, W. Huang, L. C. da Silva, K. A. I. Zhang, X. Wang, *Chem. Eur. J.* **2018**, *24*, 17454–17458.
[53] Q. Niu, Z. Cheng, Q. Chen, G. Huang, J. Lin, J. Bi, L. Wu, *ACS Sustainable Chem. Eng.* **2021**, *9*, 1333–1340.
[54] N. Xu, Y. Liu, W. Yang, J. Tang, B. Cai, Q. Li, J. Sun, K. Wang, B. Xu, Q. Zhang, Y. Fan, *ACS Appl. Energ. Mater.* **2020**, *3*, 11939–11946.
[55] A. Jati, K. Dey, M. Nurhuda, M. A. Addicoat, R. Banerjee, B. Maji, *J. Am. Chem. Soc.* **2022**, *144*, 7822–7833.
[56] H. S. Sasmal, S. Bag, B. Chandra, P. Majumder, H. Kuiry, S. Karak, S. Sen Gupta, R. Banerjee, *J. Am. Chem. Soc.* **2021**, *143*, 8426–8436.
[57] T. E. Müller, K. C. Hultzsch, M. Yus, F. Foubelo, M. Tada, *Chem. Rev.* **2008**, *108*, 3795–3892.
[58] M. Beller, J. Seayad, A. Tillack, H. Jiao, *Angew. Chem. Int. Ed.* **2004**, *43*, 3368–3398.
[59] Z. Wu, S. N. Gockel, K. L. Hull, *Nat. Commun.* **2021**, *12*, 5956.
[60] L. Hintermann, *C–X Bond Formation* (Ed.: A. Vigalok), Springer Berlin Heidelberg, Berlin, Heidelberg, **2010**, 123–155.
[61] T. Kondo, T.-a. Mitsudo, *Chem. Rev.* **2000**, *100*, 3205–3220.
[62] L. Huang, M. Arndt, K. Gooßen, H. Heydt, L. J. Gooßen, *Chem. Rev.* **2015**, *115*, 2596–2697.
[63] D. A. Petrone, J. Ye, M. Lautens, *Chem. Rev.* **2016**, *116*, 8003–8104.
[64] Y. Zhang, N. Hatami, N. S. Lange, E. Ronge, W. Schilling, C. Jooss, S. Das, *Green Chem.* **2020**, *22*, 4516–4522.
[65] Y. Qin, T. Zhang, H. Y. V. Ching, G. S. Raman, S. Das, *Chem* **2022**, *8*, 2472–2484.
[66] T. M. Monos, R. C. McAtee, C. R. J. Stephenson, *Science* **2018**, *361*, 1369–1373.
[67] T. Taeufer, R. Hauptmann, F. El-Hage, T. S. Mayer, H. Jiao, J. Rabeah, J. Pospech, *ACS Catal.* **2021**, *11*, 4862–4869.
[68] A. Petrosyan, L. Zach, T. Taeufer, T. S. Mayer, J. Rabeah, J. Pospech, *Chem. Eur. J.* **2022**, *28*, e202201761.
[69] M. Kazuhiko, N. Isao, I. Nobuyuki, O. Yoshio, *Chem. Lett.* **1989**, *18*, 1095–1098.
[70] H. Kotani, K. Ohkubo, S. Fukuzumi, *J. Am. Chem. Soc.* **2004**, *126*, 15999–16006.
[71] S. Fukuzumi, H. Kotani, K. Ohkubo, S. Ogo, N. V. Tkachenko, H. Lemmetyinen, *J. Am. Chem. Soc.* **2004**, *126*, 1600–1601.
[72] A. Tlili, S. Lakhdar, *Angew. Chem. Int. Ed.* **2021**, *60*, 19526–19549.
[73] D. S. Hamilton, D. A. Nicewicz, *J. Am. Chem. Soc.* **2012**, *134*, 18577–18580.
[74] T. M. Nguyen, N. Manohar, D. A. Nicewicz, *Angew. Chem. Int. Ed.* **2014**, *53*, 6198–6201.
[75] A. J. Perkowski, D. A. Nicewicz, *J. Am. Chem. Soc.* **2013**, *135*, 10334–10337.
[76] D. J. Wilger, J.-M. M. Grandjean, T. R. Lammert, D. A. Nicewicz, *Nat. Chem.* **2014**, *6*, 720–726.
[77] K. A. Margrey, D. A. Nicewicz, *Acc. Chem. Res.* **2016**, *49*, 1997–2006.
[78] H. Wang, Y. Man, Y. Xiang, K. Wang, N. Li, B. Tang, *Chem. Commun.* **2019**, *55*, 11426–11429.
[79] N. L. Reed, G. A. Lutovsky, T. P. Yoon, *J. Am. Chem. Soc.* **2021**, *143*, 6065–6070.
[80] H. Yi, L. Niu, C. Song, Y. Li, B. Dou, A. K. Singh, A. Lei, *Angew. Chem. Int. Ed.* **2017**, *56*, 1120–1124.
[81] X. Hu, G. Zhang, F. Bu, A. Lei, *ACS Catal.* **2017**, *7*, 1432–1437.
[82] N. P. R. Onuska, M. E. Schutzbach-Horton, J. L. Rosario Collazo, D. A. Nicewicz, *Synlett* **2020**, *31*, 55–59.
[83] N. A. Romero, K. A. Margrey, N. E. Tay, D. A. Nicewicz, *Science* **2015**, *349*, 1326–1330.
[84] N. E. S. Tay, W. Chen, A. Levens, V. A. Pistritto, Z. Huang, Z. Wu, Z. Li, D. A. Nicewicz, *Nat. Catal.* **2020**, *3*, 734–742.
[85] W. Chen, X. Wu, J. B. McManus, G. T. Bida, K.-P. Li, Z. Wu, D. A. Nicewicz, Z. Li, *Org. Lett.* **2022**, *24*, 9316–9321.
[86] J. L. Segura, R. Juárez, M. Ramos, C. Seoane, *Chem. Soc. Rev.* **2015**, *44*, 6850–6885.
[87] R. Juárez, M. M. Oliva, M. Ramos, J. L. Segura, C. Alemán, F. Rodríguez-Ropero, D. Curcó, F. Montilla, V. Coropceanu, J. L. Brédas, Y. Qi, A. Kahn, M. C. Ruiz Delgado, J. Casado, J. T. López Navarrete, *Chem. Eur. J.* **2011**, *17*, 10312–10322.
[88] X. Wang, Y. Yang, C. Lai, R. Li, H. Xu, D. H. S. Tan, K. Zhang, W. Yu, O. Fjeldberg, M. Lin, W. Tang, Y. S. Meng, K. P. Loh, *Angew. Chem. Int. Ed.* **2021**, *60*, 11359–11369.
[89] Y. Wang, Z. Qiao, K. Liu, L. Yu, Y. Lv, L. Shi, Y. Zhao, D. Cao, Z. Wang, S. Wang, S. Yuan, *Adv. Sci.* **2022**, *9*, 2205069.
[90] J. Yin, N. Li, M. Liu, Z. Li, X. Wang, M. Cheng, M. Zhong, W. Li, Y. Xu, X.-H. Bu, *Adv. Funct. Mater.* **2023**, *33*, 2211950.
[91] X. Yang, L. Gong, X. Liu, P. Zhang, B. Li, D. Qi, K. Wang, F. He, J. Jiang, *Angew. Chem. Int. Ed.* **2022**, *61*, e202207043.
[92] V. B. Saptal, V. Ruta, M. A. Bajada, G. Vilé, *Angew. Chem. Int. Ed.* **2023**, *62*, e202219306.
[93] C. Wang, H. Zhang, W. Luo, T. Sun, Y. Xu, *Angew. Chem. Int. Ed.* **2021**, *60*, 25381–25390.
[94] Z. Yang, H. Chen, S. Wang, W. Guo, T. Wang, X. Suo, D.-e. Jiang, X. Zhu, I. Popovs, S. Dai, *J. Am. Chem. Soc.* **2020**, *142*, 6856–6860.
[95] F. Haase, K. Gottschling, L. Stegbauer, L. S. Germann, R. Gutzler, V. Duppel, V. S. Vyas, K. Kern, R. E. Dinnebier, B. V. Lotsch, *Mater. Chem. Front.* **2017**, *1*, 1354–1361.
[96] F. Auras, L. Ascherl, A. H. Hakimioun, J. T. Margraf, F. C. Hanusch, S. Reuter, D. Bessinger, M. Döblinger, C. Hettstedt, K. Karaghiosoff, S. Herbert, P. Knochel, T. Clark, T. Bein, *J. Am. Chem. Soc.* **2016**, *138*, 16703–16710.
[97] X. Chen, M. Addicoat, S. Irle, A. Nagai, D. Jiang, *J. Am. Chem. Soc.* **2013**, *135*, 546–549.
[98] J. Yang, A. Acharjya, M.-Y. Ye, J. Rabeah, S. Li, Z. Kochovski, S. Youk, J. Roeser, J. Grüneberg, C. Penschke, M. Schwarze, T. Wang, Y. Lu, R. van de Krol, M. Oschatz, R. Schomäcker, P. Saalfrank, A. Thomas, *Angew. Chem. Int. Ed.* **2021**, *60*, 19797–19803.

Manuscript received: August 15, 2024
Accepted manuscript online: October 15, 2024
Version of record online: November 16, 2024